Experimentally validated numerical model of coupled flow, thermal and electromagnetic problem in small power electric motor

Lukasz Slupik, Jacek Smolka

Institute of Thermal Technology, Silesian University of Technology
Konarskiego 22, 44-100 Gliwice, Poland
e-mail: lukasz.slupik@polsl.pl, jacek.smolka@polsl.pl

Luiz C. Wrobel

School of Engineering and Design, Brunel University
Uxbridge UB8 3PH, United Kingdom
e-mail: luiz.wrobel@brunel.ac.uk

This paper describes results of the mathematical modelling of the steady-state thermal phenomena taking place in a Fracmo 240 W DC electric motor. The model of the motor was defined in the ANSYS Fluent software to predict flow and temperature fields inside the machine. The thermal model was coupled with an electromagnetic solver to determine power losses occurring in different parts of the unit. In order to validate the proposed numerical model, a test rig was set up to measure temperatures at points located inside the motor housing and on its external wall. Additionally, the temperature field was captured by an infrared camera. The results obtained from the coupled analysis are comparable with the measurement data.

Keywords: computational fluid dynamics, coupled thermal problems, electric motor, validation.

1. INTRODUCTION

There is an increasing pressure on electrical motor manufacturers nowadays to develop smaller, more energy-efficient electric motors. This can be achieved with the help of accurate thermal models, which are presently indispensable in motor design process [15]. Very often, for better economy, the motor needs to operate close to, but not above, the thermal limitation for its insulation. This leads to the need for more accurate performance predictions [8]. There are two basic types of thermal analysis of electric motors: analytical lumped-circuit and numerical methods. In [2], the authors explained in detail each method and additionally presented an extended review and a summary of the modern thermal analysis of electric motors. In particular, they focused on computational fluid dynamics (CFD), finite element method and lumped parameter thermal network analysis. Each method was compared and their strengths and weaknesses were discussed. One of the earliest CFD analyses of the thermal performance of a small electric motor was presented in [9]. Finite element software combined with double chamber calorimeter (DCC) was used to estimate main power losses inside the motor. Finally, the Fluent software was adopted to determine the temperature distribution within the motor, and it was shown that the results of the test and computations were comparable. For some manufacturers, the thermal stability of the motor is considered as the most important design factor. This problem was verified in [7] by both CFD and thermal equivalent circuit methods and the results from these two methods were compared to the test data and validated.

Reference [16] deals with the combined thermal network and CFD analyses of an induction machine. CFD was used to deal with convective heat transfer while the analytical thermal network approach was used to calculate conduction in the electromagnetic structure. Several interesting papers have been published in recent years on thermal analysis of electric motors. For instance, in [5] the thermal performance of a large scale motor is investigated both numerically and experimentally. Moreover, the authors show that accurate modifications in the design can lead to a temperature decrease in both stator and rotor. The main advantage of CFD over thermal network analysis is that it can be used to predict flow in complex regions, such as around and inside the motor. This is why the CFX code was used in [3] to investigate the external air flow in a totally enclosed fan cooled electric motor. The same author presents in [4] the CFD evaluation of the airflow around the end winding section of an asynchronous motor.

This paper presents results of the CFD analysis of the Fracmo 240 W DC motor in steady-state condition. The first stage of the modelling was to create a very complex motor geometry using the CATIA [12] software and then to implement it in the Gambit [6] code. The geometrical model was simplified with the objective of making the geometry periodic. Only one quarter of the motor was numerically modelled and the concept of rotational periodic boundary condition was used. The SPEED [13] software was used to determine the main power losses inside the motor. Finally, the model of the motor has been implemented in the ANSYS Fluent software package [17] to predict the flow and thermal fields inside the DC motor.

2. Thermal measurements of electricmotor

In order to create a numerical model of the electric motor, which adequately represents the real motor, a number of measurements were performed to determine the temperature field within the machine under consideration. The temperature was captured by an infrared camera and, to do so, the motor was painted with a black paint of known emissivity.

The measurements were performed on the test rig presented in Fig. 1. The motor painted black is the tested one and it is powered by a battery pack. The mechanical energy produced in the tested motor was converted back to electric in the second motor, which works as an electric generator. In the resistors (the green ones), electric energy was finally converted into heat.
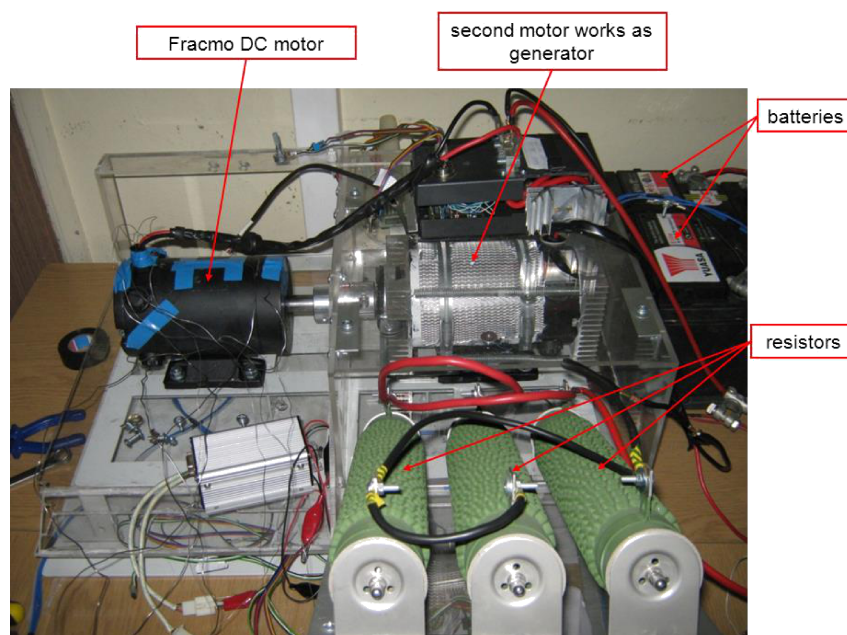

Fig. 1. A general view of the test rig.

Measurements of the temperature field were experimentally performed in order to verify the motor operation under a current load of 9.3 A. The temperatures were measured using the type T. The sensors were mounted at different locations and were recorded by a data recorder. The layout of the thermocouples mounted on the motor is shown in Fig. 2.
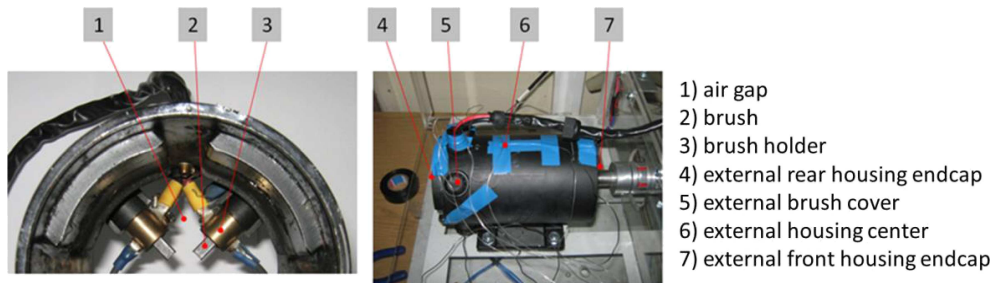

1) air gap
2) brush
3) brush holder
4) external rear housing endcap
5) external brush cover
6) external housing center
7) external front housing endcap

Fig. 2. Schematic layout of the thermocouples on the Fracmo DC motor.

During measurements the motor current and voltage were close to the nominal parameters for this machine. Figure 3 illustrates the temperature variation in time. It can be observed that the steady state condition was reached for all seven measuring points, as all curves reached their horizontal asymptotes. The brush and the brush holder present the highest temperature values as a result of the existence of two different heat sources that appear within the brush. The first one refers to the friction generation between the commutator and the brush surface, while the second refers to the heat generation within the brush as a result of the current flow. This type of heat generation is also known as Joule heat.

Air inside the machine was completely enclosed within a tight housing and also had a high temperature. The remaining thermocouples were mounted on the external wall of the housing, where the temperature is of course much lower. The main goal of the experiment was to reach a steady-state condition. These temperatures were later used to validate the numerical model.
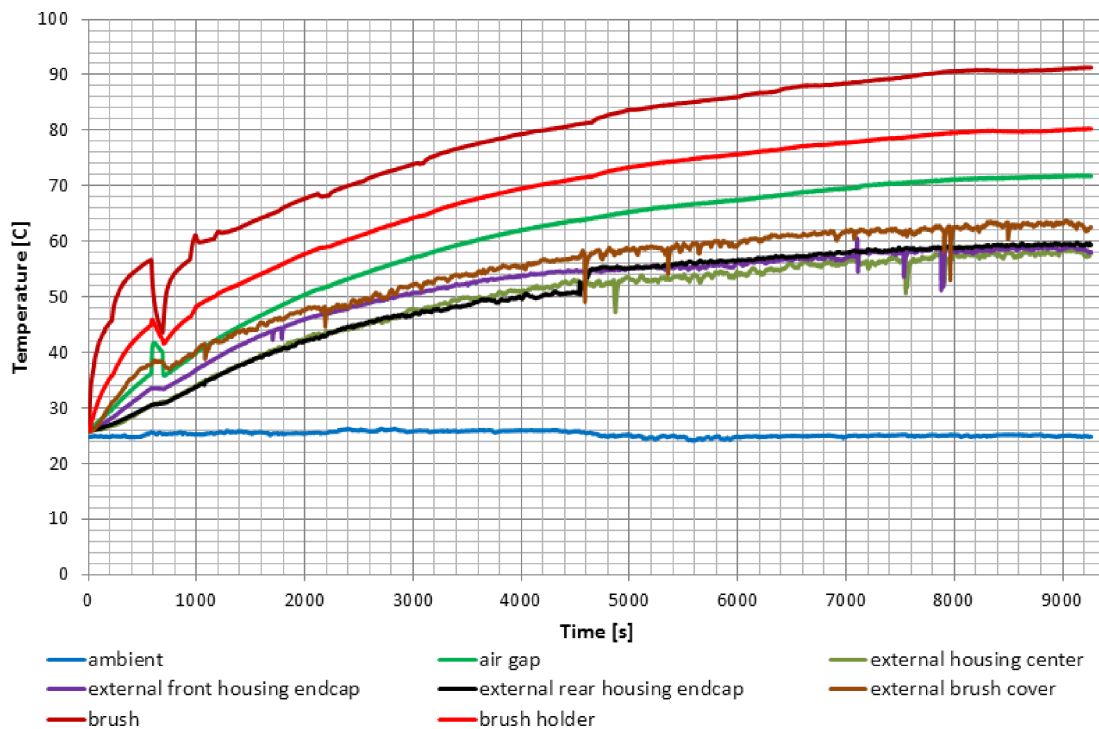

Fig. 3. Graph of the motor heating.

Additionally, the temperature was captured using the infrared camera, see Fig. 4. Due to the Joule heating and the friction generation in the brush, the hot-spots on the motor surfaces were at the plastic cap cover. It was also noticed that the temperature field was almost uniform only with the region corresponding to the housing end cap rear and the brush cap a little bit higher than the rest of the motor surface.
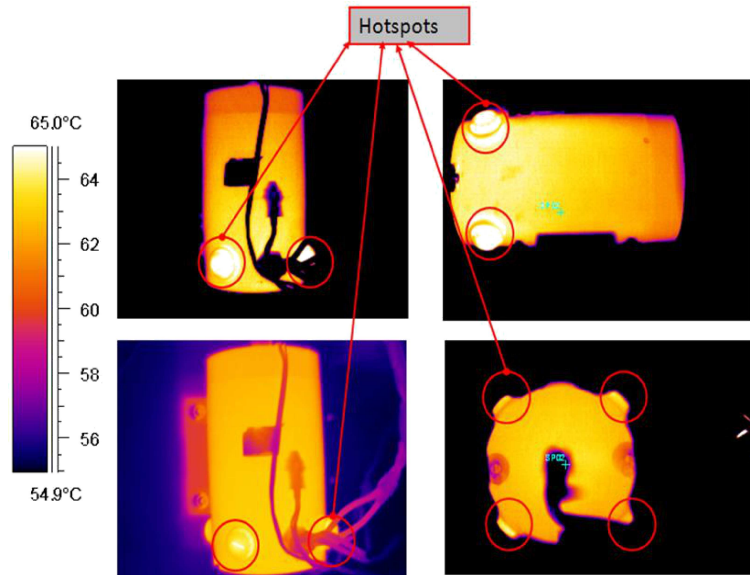

Fig. 4. Infrared camera pictures of the Fracmo DC motor.

3. Geometry and mesh of fracmo DC motor

The Fracmo DC 240 W motor is a permanent-magnet DC commutator machine. This type of motor is widely used in automotive applications (windscreen wipers, heater blowers, cooling fans), where the supply is low-voltage DC at 12 V (24 V in trucks). Because of their excellent control characteristics these motors are also widely used in low-power motion control applications, where they can be controlled with low-cost electric drives such as choppers and phase-controlled converters [13].

As shown in Figs. 5 and 6, the electric motor model has a very complicated geometry. Obviously, it was difficult to model the entire machine with all the details. Additionally, the motor elements which were neglected are not significant for the heat transfer and fluid flow within the machine. The motor geometry was created with the CATIA software.
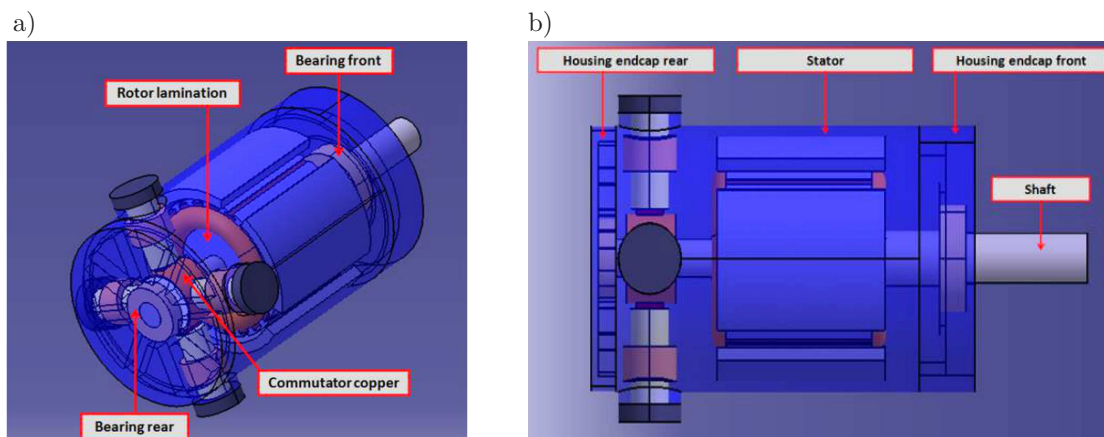

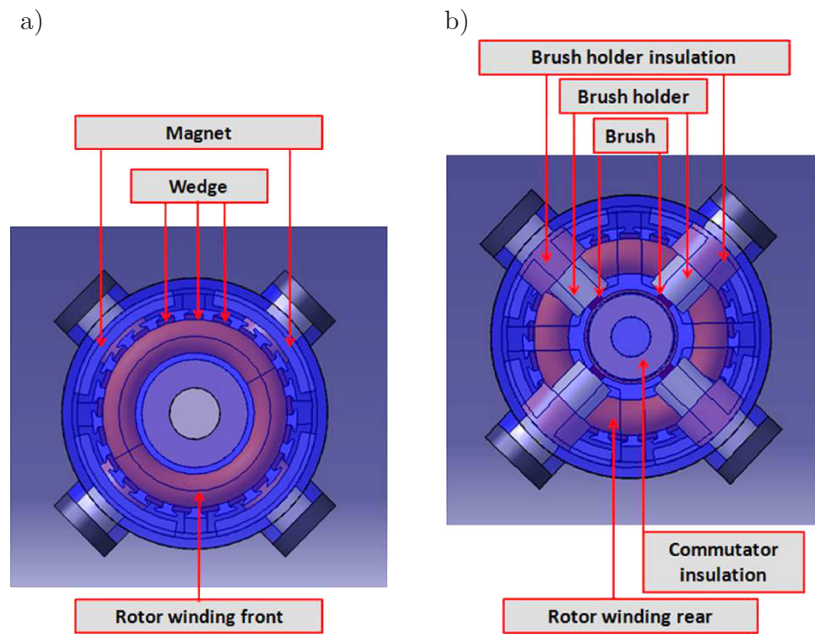**Fig. 5.** (a) Isometric and (b) top view of the Fracmo DC motor.

Fig. 6. View of Fracmo DC motor: a) front, b) rear.

The main geometric simplifications were related to the rotor itself. In terms of geometry, the rotor was the most difficult element to model, as it can be seen in Fig. 7. The main assumptions were as follows:

- To make the geometry fully periodic, the number of slots within the rotor was decreased from 21 to 20.

- Due to the geometry complexity and problems with the mesh generation, the air gaps between slots were not modelled. As it can be seen in Fig. 7, the gaps were filled with a solid which represents steel. It seems that this assumption can be justified having in mind a thin layer of the air gap between the rotor and the stator and a relatively high speed of rotation. Simply, the heat is mostly transferred in a radial, not in a tangent direction.

- The end winding region was modelled as a torus. This simple shape made this particular region easier to mesh, and additionally, it fulfilled the rotational periodic condition.
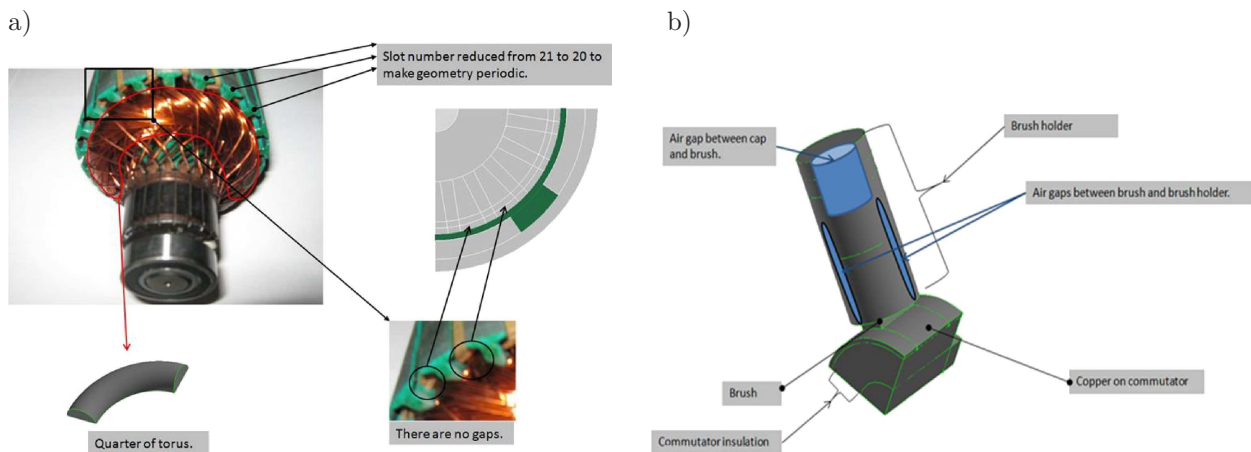

Fig. 7. (a) The rotor simplifications and (b) model of the brush and the commutator.

- The wires connecting the commutator and the rotor were not modelled, due to the geometry and problems related to mesh generation.

- Taking into consideration the above mentioned simplification, only one quarter of the model was considered, because the geometry and the boundary conditions were symmetric.

- The commutator was modelled as a thin slice of the copper that covers the insulation, which is located behind it.

- As it can be seen in Fig. 7, small air gaps exist between the brush, the brush holder and the cap. These gaps were not modelled because of their small sizes and problems related to mesh generation. Moreover, the gaps are totally or partially enclosed so the air motion in those regions does not exist or is limited during the motor operation. During the simulation these particular regions were defined as a solid domain with the effective thermal conductivity, which takes the thermal resistance of the air into account.

- The bearings were modelled as one single solid part.

- The air around the motor was modelled by adding an additional volume with pressure outlet boundary condition.

As shown in Fig. 8, the mesh for the motor was created based on tetrahedral elements, as these are the only elements capable of meshing that domain. Due to the complexity of the geometry and to reduce mesh size, only one quarter of the geometry was considered because geometry and boundary conditions were symmetric. The meshes were built in such a way that zones of greater interest like the air gap between rotor and stator, the rotor, the commutator and brush region were meshed with a finer mesh. In order to reduce the number of elements between the motor and the volume which represents air, the size function was used.
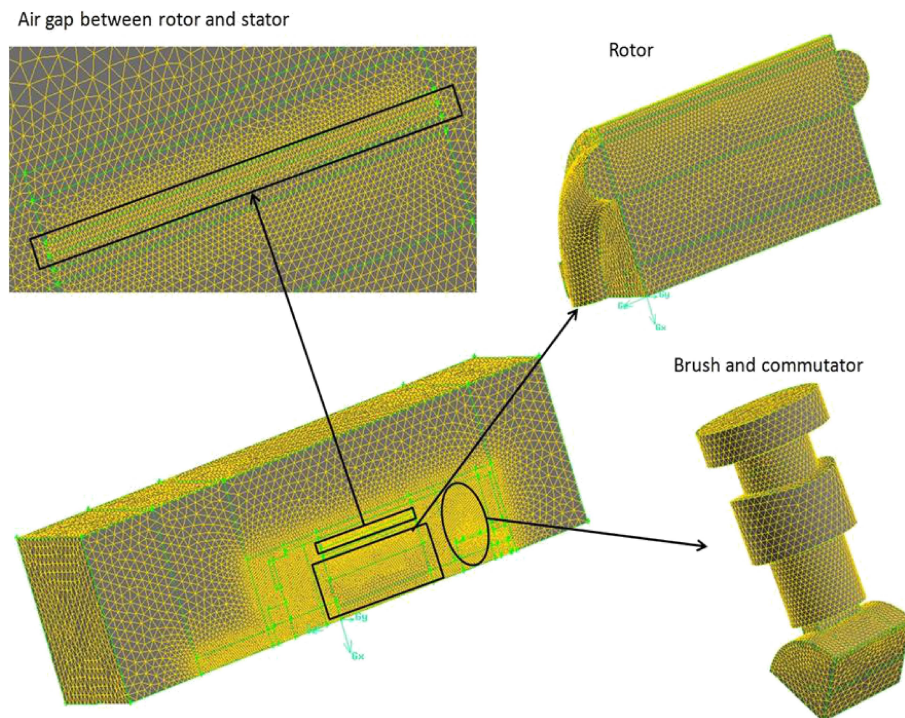

Fig. 8. A general view of the final mesh.

A mesh sensitivity test was performed in order to find the optimal mesh for the final model. The meshes were created in such a way that the interval size of each tetrahedral element was increased

by 20% from elements in the previous grid. In order to do so, six tetrahedral meshes were created and they are listed in Table 1. Simulations were performed for the voltage of 24 V and the current of 9.3 A.

Table 1. Temperature values at measurement points: I – air gap, II – brush, III – brush holder, IV – external rear housing end cap, V – external brush cover, VI – external housing centre, VII – external front housing end cap.

Mesh	Number of elements	I, °C	II, °C	III, °C	IV, °C	V, °C	VI, °C	VII, °C
1.	560 703	73.79	90.24	84.14	64.03	62.96	61.31	60.33
2.	792 607	74.23	90.46	84.44	64.49	63.42	61.78	60.71
3.	1 184 999	74.07	90.25	84.16	64.32	63.24	61.62	60.59
4.	**1 619 736**	**73.80**	**89.68**	**83.53**	**63.97**	**62.88**	**61.28**	**60.26**
5.	2 557 000	73.85	89.37	83.40	63.96	62.88	61.30	60.31
6.	3 489 323	74.83	90.89	84.73	64.99	63.94	61.26	61.23

From the results obtained for meshes 1–6, it becomes obvious that the solution did not differ significantly. The difference in the solutions does not exceed 1.5 K. It was decided that mesh number 4, consisting of over 1.6 million elements, would be used to simulate heat transfer and fluid flow within the DC motor. Such a decision was made to ensure a good representation of the physical values that will be presented later on.

4. MATHEMATICAL MODEL

The main governing equations of the mathematical model presented in this work can be easily found in CFD textbooks, *e.g.*, [1, 11]. Nevertheless, the fundamental equations are listed below together with some brief information on physical unknown that is calculated when solving a particular equation. Hence:

- The Fourier-Kirchhoff equation is solved for the temperature in both fluids as well as in solid walls. In fluids, this equation reads

$$\nabla \cdot (k \, \nabla T) + S_h = c_p \rho \, \mathbf{v} \cdot \nabla T, \tag{1}$$

  where k is for the thermal conductivity, T is temperature, S_h is the source term, c_p is for isobaric specific heat, ρ is the density and $\mathbf{v}$ is the velocity vector.

- The Navier-Stokes equation, also called momentum equation, is solved for the velocity vector $\mathbf{v}$ only in fluids,

$$\nabla \cdot (\rho \, \mathbf{vv}) - \nabla p + \rho \, \mathbf{g} = 0, \tag{2}$$

  where p is the pressure and $\mathbf{g}$ is gravity acceleration.

- The continuity equation is solved for pressure only in fluids,

$$\nabla \cdot (\rho \, \mathbf{v}) = 0. \tag{3}$$

- There are several different turbulence models available in Fluent [13]. Taking into account the characteristics of the flow and suggestions of the Fluent Manual, the standard κ - ε model has been used,

$$\begin{aligned}
\rho \, (\mathbf{v} \cdot \nabla \kappa) &= \nabla \cdot [(\mu + \mu_T/\mathrm{Pr}_k) \, \nabla \kappa] + S \, (\mu_T, \, \kappa, \, \mathbf{v}) \\
&\quad - \rho \, \varepsilon \\
\rho \, (\mathbf{v} \cdot \nabla \varepsilon) &= \nabla \cdot [(\mu + \mu_T/\mathrm{Pr}_\varepsilon) \, \nabla \varepsilon] + C_{\varepsilon 1} \, \frac{\varepsilon}{\kappa} S \, (\mu_T, \, \kappa, \, \mathbf{v}) - C_{\varepsilon 2} \, \rho \, \frac{\varepsilon^2}{\kappa}
\end{aligned}, \tag{4}$$

where μ is the molecular dynamic viscosity, μ_T is for turbulent dynamic viscosity, κ is the turbulence kinetic energy, ε is the rate of turbulence kinetic energy dissipation and Pr is the Prandtl number.

- The radiative transfer equation (discrete ordinate model [1]) is solved for radiative heat fluxes on the surfaces of solid walls,

$$
\frac{\mathrm{d}i\left(\mathbf{r}, \xi\right)}{\mathrm{d}\xi} = -\, a\, i\left(\mathbf{r}, \xi\right) + a\, i_b\left(\mathbf{r}, \xi\right)
$$
$$
\dot{q}_r = a \int\limits_{\omega = 4\pi} \left(i - i_b\right)\, \mathrm{d}\omega \qquad \dot{q}_{v,r} = -\nabla \cdot \dot{q}_r
$$

(5)

where i is the intensity, i_b is the black body intensity, a is absorption coefficient and ω is the solid angle.

It needs to be mentioned that the computational domain consists of two types of materials, which are the solid parts $e.g.$, stator, rotor, housing, and the fluid represented by air gaps inside the machine. Thermal properties of the solid parts were set based on a material database for a typical low-power DC motor that is available from the demo version of the Motor-CAD software [10]. Moreover, the total heat flux including the convective and the radiative parts was defined on the external walls of the motor housing.

5. Heat generation

It is imperative that the heat losses in the machine and their distribution need to be known in order to obtain a good prediction of the temperatures throughout the machine. Some losses are associated with the electromagnetic design (copper, iron), others like friction and windage are associated with the mechanical design [14]. In this particular DC machine, windage losses did not exist because the housing of the motor was totally enclosed. There are four sources of power losses that occur within the motor under consideration: copper, iron, friction, brush.

Some machines have stator copper losses and some others rotor copper losses. Some have both. In this particular case, the rotor copper losses existed. The copper losses were active and the end winding section can be calculated based on the amount of material in both sections. The copper properties depend on current and temperature. The increase in winding temperature gave an increase in copper resistivity. The torque in a permanent magnet motor is proportional to the current, and an increase in the current will give an increase in the copper losses proportional to the square of the current. Taking into account the model under consideration, the copper losses were generated within the rotor windings.

The iron losses were calculated using the modified Steinmentz equation, which takes into account the variation of the flux-density in the teeth and the rotor core as the rotor rotates. The iron losses were calculated as no-load values, and no account is taken of their variation with load [13]. The iron losses have been attached to the rotor lamination. It should be mentioned that it is difficult to calculate iron losses accurately because losses data from the material manufacturer may not have the same situation as in the working machine.

The friction losses existed mainly between brush and commutator surface. Friction is also generated within the bearing, however if we take under consideration the infrared camera pictures presented below, it can be observed that the temperature was uniform on both housing end caps. There are no hot-spots, which indicate significant friction generation within the bearing. Thus, all friction losses in the numerical simulation were attached and generated in the commutator-brush region.

The heat generation within the brush was a result of the current flow. These losses were divided in such a way that only 5% of the friction was attached to the volume representing copper that
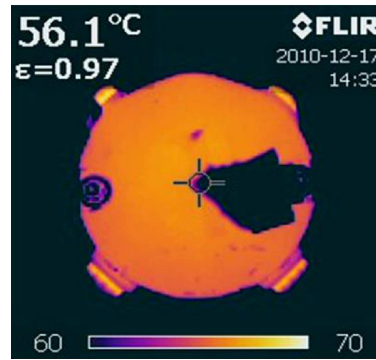
Fig. 9. The infrared picture of the motor rear.

covers the commutator. The rest of it (95%) was applied to the brush as a boundary condition of the second kind.

The analytical electromagnetic simulations, based upon classical theory and the equivalent circuit method, were performed in the SPEED software to determine the main power losses in the Fracmo DC motor. The results of the analysis are presented in Table 2.

Table 2. Heat loss types calculated using SPEED for current 9.3 A
and angular velocity 2006 rpm.

Copper, W	Iron, W	Friction, W	Brush, W
22.22	3.19	21.00	6.70

The main sources of losses were typically copper and iron. However, if we take under consideration values of iron losses presented in Table 2, it becomes clear that the iron losses were underestimated and additionally the friction losses were overestimated. It seems that SPEED gives a low prediction of iron losses. This is typical when data is provided by the steel manufacturer. During the calculation, an adjustment factor called X_{fe} was left as default ($X_{fe} = 1$) because it was difficult to find its value for this particular type of the motor. Instead, a large number of CFD simulations were performed in order to find the correct combination of friction and iron losses. Finally, the friction losses were decreased to 70%, while the iron losses were increased by adding 30% of the friction losses. Such a solution makes the energy balance unchanged and provides better results that are close to the measurement data. Finally, the new combination of power losses is listed in Table 3.

Table 3. Heat loss types recalibrated for current 9.3 A
and angular velocity 2006 rpm.

Copper, W	Iron, W	Friction, W	Brush, W
22.22	9.49	14.70	6.70

6. RESULTS AND DISCUSSION

All stages were simulated for steady-state conditions with standard k-ε turbulence model with first-order upwind scheme. Moreover, the effect of the rotor rotation was omitted. In order to present temperature fields in the entire model, the results are periodically repeated four times, because the model includes only one-fourth of the real unit.

As it was mentioned in Sec. 2, during the measurement phase a thermal image of the motor was captured using the infrared camera. This image allows one to compare experimental results with those obtained from the CFD simulation, as shown in Fig. 10. In the infrared thermal image the
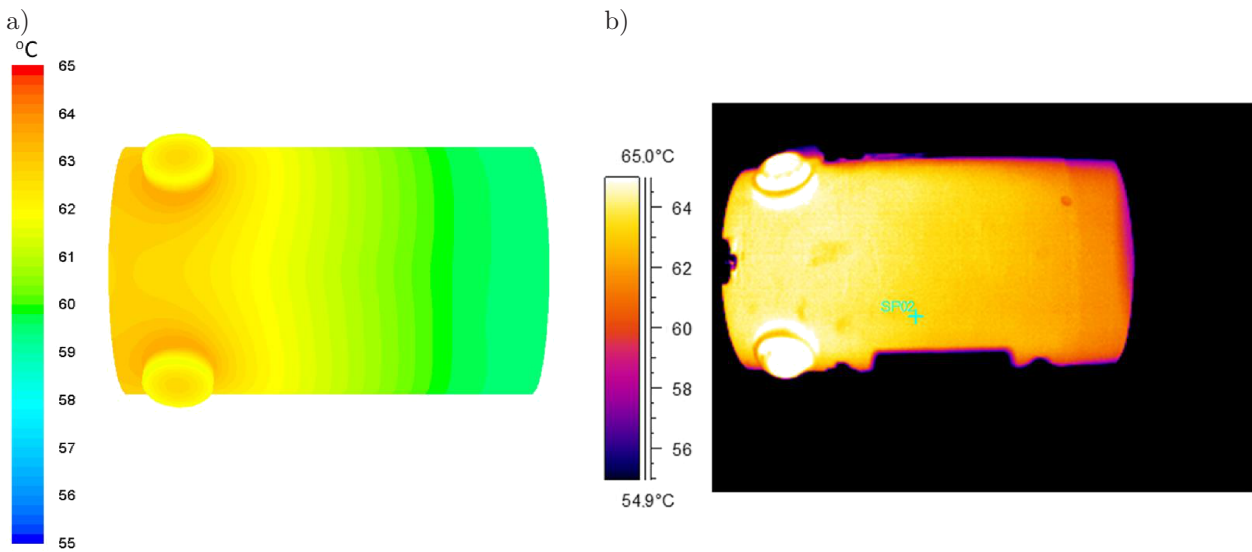
a)

b)

Fig. 10. Temperature field in °C on the housing surface from (a) the steady-state simulation and (b) the infrared camera image.

hot-spot region corresponds to the cap covering the brush, while in the CFD result this effect is not notable. Moreover, it can be noticed that the temperature obtained via infrared measurements differs between end cap front and end cap rear by about 9 K, while in the CFD simulation the difference is smaller than 3 K. This may indicate that copper losses, which correspond to the rotor, were overestimated in the numerical model.

To better demonstrate thermal processes within the motor under consideration, four radial cross-section planes were used in Fig. 11. The temperature scale was narrowed in order to show the thermal processes which occur within the rotor. Firstly, it can be seen that the rotor was heated due to the rear region where the brush and friction losses occur. Within the rotor, periodically repeated hot-spot regions can be observed. These particular regions of the rotor were originally filled with windings which were, of course, the main heat source within the rotor. The shaft from the front is conducting heat into the housing end cap rear, therefore a lower temperature can be observed in the centre of the first plane.
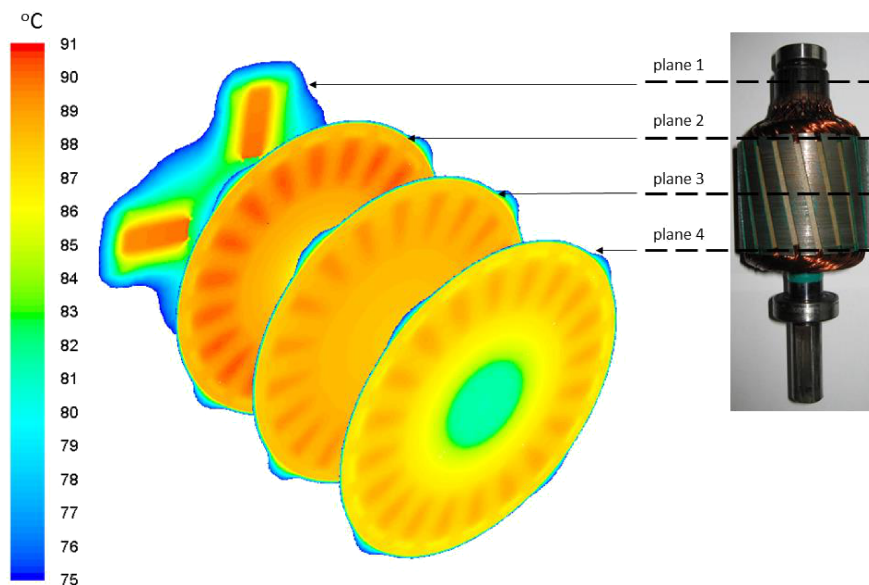

Fig. 11. Temperature field in °C on four radial cross-sections of the motor.

Analysing the temperature field in Fig. 12, it can be observed that, within the rotor, a significant amount of heat was generated due to the existence of the copper winding. The brush and brush holder were the second location where hotspots can be noticed. This corresponds to the current flow through the brush into the commutator and additional friction generation between commutator and brush surface. The rotor end regions are places of strong accumulation of the copper winding, causing a small round hot spot on the rotor right ending to be observed. Due to friction and Joule heat generation within the brush section, the rotor temperature is not uniform. Brush and brush holders play the main role in the heat conduction into the housing. Additionally, it can be noticed that the shaft conducted most of the heat generated within the rotor to the housing front and rear regions. Finally, from the housing, the heat was released to the ambient by natural convection and radiation.
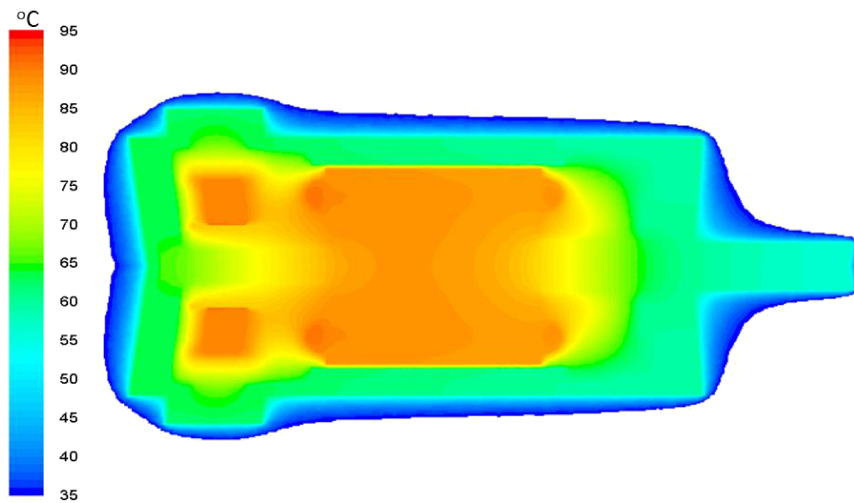

Fig. 12. Temperature field in °C on the longitudinal cross-section of the motor.

As mentioned earlier, the temperature was measured at seven points by thermocouples. Values of temperatures at the measuring points for the motor are presented in Table 4. The differences between measurements and CFD simulation are small and do not exceed 4 K.

Table 4. Result of the calculations of the temperature field of the Fracmo DC motor.

Measurement point	Measured temperature, °C	Calculated temperature, °C
Air gap	71.5	73.8
Brush	91.3	89.7
Brush holder	80.3	83.5
External rear housing end cap	62.6	64.0
External brush cover	59.4	62.9
External housing center	57.8	61.3
External front housing end cap	58.1	60.3

7. Conclusions

This article experimentally and numerically investigated thermal processes that occur within a small power Fracmo 240 W DC motor. The results of the coupled thermal and electromagnetic simulation performed for the motor were comparable with the measurements. The comparison between the CFD simulation and the thermal image obtained by the infrared camera shows some

similarities like, for example, hot-spots located in the same places. The motor in its rear region was heated more than in the front region. From the CFD temperature field pictures it can be concluded that the heat is generated mainly within the rotor winding, brush and commutator. The rotor plays one of the main roles, conducting the heat generated in the rotor to the housing. From the housing, heat was released to the ambient by natural convection and radiation. Additionally, it has been confirmed that the rotor is heated unevenly.

The proposed CFD model of a small power electric motor can be used to predict heat transfer and fluid flow in complex regions such as the end winding and the air gap between rotor and stator. Moreover, the heat transfer coefficient and average temperature values of each component inside the machine can also be obtained. As a consequence, these values can be implemented in commercial circuit software such as Motor-CAD [10].

ACKNOWLEDGMENT

REFERENCES

[1] J.D. Anderson Jr. *Computational Fluid Dynamics. The Basics with Applications*, McGraw-Hill, USA, 1995.
[2] A. Boglietti, A. Cavagnino, D. Staton, M. Shanel, M. Mueller, C. Mejuto. *Evolution and Modern Approaches for Thermal Analysis of Electrical Machines*. IEEE Trans. Ind. Electron., **56**(3), March 2009.
[3] C.A. Cezario, A.A.M. Oliveira. *Electric motors external fan system CFD validation*. Proc. IEEE Int. Conf. Elect. Mach., 2008.
[4] C.A. Cezario, A.A.M. Oliveira. *Electric motors internal fan system CFD validation*. Proc. IEEE Int. Conf. Elect. Mach., 2008.
[5] C.-C. Chang, Y.-F. Kuo, J.-C. Wang, S.-L. Chen. *Air cooling for a large-scale motor*. Applied Thermal Engineering, **30**: 1360–1368, 2010.
[6] GAMBIT 2.4 User's Guide. Fluent, Inc., May 2007.
[7] W.-G. Kim, J.-I. Lee, K.-W. Kim, Y.-S. Kim, C.-D. Lee. *The temperature rise characteristic analysis technique of the traction motor for EV application*. IFOST, 18–20 Oct. 2006.
[8] D. Lampard, S.J. Pickering, J. Mugglestone. *The use of computational fluid dynamics to model the air flow in the end region of a TEFC induction motor*. IEE, London, 1997.
[9] W. Mei, M.A. Jabbar, A.O. Tay. *Determination of thermal performance of small electric motors*. IEEE PEDS, Indonesia, 2001.
[10] Motor-CAD. [Online]. Available: www.motor-design.com.
[11] A.J. Nowak. *Numerical Heat Transfer*, Gliwice, Poland, 2009.
[12] K. Plantenberg. *Introduction to CATIA V5 Release 19*, 2009.
[13] *SPEED's Electric Motors*. TJE Miller, University of Glasgow, 2008, Private correspondence.
[14] D. Staton. *Losses in Electrical Machines – Thermal Training*, Private correspondence.
[15] D. Staton, D. Hawkins, M. Popescu. *Motor-CAD Software for Thermal Analysis of Electrical Motors – Links to Electromagnetic and Drive Simulation Models*. CWIEME, Berlin, June 2010.
[16] F.J. Trigeol, Y. Bertin, P. Lagonotte. *Thermal modelling of an induction machine through the association of two numerical approaches*. IEEE Trans. Energy Convers., **21**(2): 314–323, Jun. 2006.
[17] *User's guide of ANSYS Fluent 12*. Release 12.0, ©ANSYS, Inc., 2009.